Impulse identification technique by estimating specific modal ponderations from vibration measurements

Dimitri Goutaudier, Didier Gendre, Véronique Kehr-Candille, Roger Ohayon

Impulse identification technique by estimating specific modal ponderations from vibration measurements

Dimitri Goutaudier[a,b,c,*], Didier Gendre[b], Véronique Kehr-Candille[a], Roger Ohayon[c]

[a] *Onera, Department of Materials and Structures, Châtillon, France*
[b] *Airbus, Airport Operations, Blagnac, France*
[c] *Cnam, Structural Mechanics and Coupled Systems Lab., Paris, France*

Abstract

Impact identification is a major concern in structural health monitoring. It consists in localizing the impact point and in reconstructing the applied load history from indirect measurements. However, it is well-known that this double inverse problem is ill-posed. In this paper, a single-sensor approach for quickly localizing a Dirac-like impact and for estimating its intensity from vibration measurements is proposed. It is proved that the relative proportions of specific modal ponderations are a signature of impact location. Rules are provided to select the appropriate vibration modes in the analysis and to position the sensor. The identification process is robust if the vibration modes kept in the analysis are weakly damped and if their natural frequencies are well separated. Experiments are conducted on a metallic plate to validate this single-sensor approach on a 2D structure. The success rate for localizing impacted cells is 100% when appropriate method parameters are selected.

Keywords: Structural health monitoring, impact identification, impact localization, inverse problem

1. Introduction

Real-time reporting of impact events allows to monitor the structure's integrity during its operating conditions. However, direct measurement of the loads acting on the structure are often unavailable, mainly because impact location is undetermined. Inverse methods must be employed to identify both the impact location and the applied load history from vibration measurements of a limited number of sensors. Numerous researches have been conducted for impact localization and load identification by assuming a linear elastic behavior and a point impact. Both the localization problem and the reconstruction problem are known to be ill-posed [1]. A small perturbation of the data, such as measurement noise or modelling errors, may lead to a completely erroneous identification. Two approaches are investigated in the scientific literature to deal with this double inverse problem.

The first approach consists in localizing the impact point before reconstructing the load history. The impact location can be triangulated by estimating the Time-Of-Flights (TOFs) of some elastic waves at different points of the structure. Ahmari and Yang [2] numerically validated a triangulation technique on a simply supported metallic plate virtually equipped with 12 displacement sensors. They used an analytical propagation velocity model of flexural waves to translate the TOFs into distances in order to localize the simulated impacts. Zhao et al. [3] considered the propagation of the fundamental anti-symmetric Lamb wave mode A_0 in a Carbon Fiber Reinforced Polymer (CFRP) plate equipped with four strain gauges in its corners. They estimated the TOFs with a wavelet transform to reduce the influence of the measurement noise. The triangulation problem is formulated with a non-linear set of equations depending on the propagation angles.

*Corresponding author
Email address: dimitri.goutaudier@gmail.com (Dimitri Goutaudier)

They developed a numerical procedure combining a particle swarm optimization algorithm and a genetic algorithm to solve it. Frieden et al. [4] proposed to use an experimental reference data set to build the velocity model of A_0 waves traveling in a composite structure. They experimentally validated their technique on a clamped CFRP plate equipped with four accelerometers or FBG sensors located in the corners of the plate.
The applied load history can be reconstructed once impact location is known. With the assumptions of a linear elastic behavior and a point impact, the reconstruction problem becomes a linear deconvolution problem [5]. However, this problem is ill-conditioned and a regularization technique must be employed [6]. Chen and Chan [7] used the Truncated Singular Value Decomposition (TSVD) to reconstruct dynamic loads acting on a bridge deck. The regularization parameter was the number of removed singular values. Tikhonov regularization [8] is also commonly employed to regularize the reconstruction problem. Khalori et al. [9] used the L-curve method [10] to determine the optimal Tikhonov regularization parameter. They experimentally validated this technique to reconstruct impact loads applied on a steel-beam-reinforced concrete deck. However, Jacquelin et al. [11] pointed out that the L-curve method becomes tricky in the case of multiple corners. Generalized Cross Validation (GCV) is another commonly used technique to estimate the regularization parameter [12]. Choi et al.[13] compared the L-curve method and the GCV technique to numerically reconstruct impact forces applied on a simply supported plate. The L-curve technique was shown to give better results for noisy data while GCV methods were better for lightly noised data. Eventually, l_1 regularization [14] can be considered to estimate impact loads that are characterized by a very short duration. Hence the reconstruction problem consists in the estimation of a sparse vector. Qiao et al. [15] experimentally validated this technique on a composite wind turbine blade and on a shell structure.

The second approach consists in simultaneously solving the localization problem and the reconstruction problem. Mainly three techniques have been developed to this end. Firstly, sweeping techniques consist in solving the reconstruction problem on a grid of candidate impact points defined on the structure. The candidate of the grid that leads to the minimization of a distance between predictions and measurements is selected as the impact point. Li and Lu [16] simultaneously identified the impact point and the applied load history on a clamped beam equipped with two accelerometers. They solved the reconstruction problem on a grid of evenly spaced candidates with Tikhonov regularization and the L-curve method. A quadratic distance was used to compare the predictions with the measurements. Vladislav et al. [17] numerically validated the same sweeping technique with a finite elements model of a metallic panel with a hole. The grid of candidates was the mesh of the model. They proposed an interpolation technique to refine the localization of the impact point. Secondly, techniques based on modal ponderations consist in estimating the contributions of some vibration modes in the response as a signature of impact location. Briggs and Tse [18] proposed to build an experimental data set to link a few modal ponderations to impact location and intensity. They assumed that the frequency spectrum of applied load history was flat in the frequency band of the selected vibration modes. They experimentally validated their technique on a beam-like structure equipped with one accelerometer only. The four first vibration modes were kept in the analysis but no general rule was provided regarding this choice. Wang and Chiu [19] developed a similar technique in time domain to simultaneously identify impact location and intensity. They proved that modal ponderations are linked to the lines of the modal matrix. They proposed a least-squares procedure to simultaneously estimate impact intensity and modal ponderations. They experimentally validated their technique on a simply supported beam equipped with one accelerometer only. They observed that the accelerometer location had a strong influence on the accuracy of the impact identification. In particular, multiple impact locations were identified if the accelerometer was close to a modal node. Eventually, non-model based techniques have been developed to simultaneously identify impact location and some load history parameters. Zhong et al. [20] trained a neural network to localize impacts applied on a stiffened composite panel and to estimate the impact energy.

The objective of this work is to develop an accurate and robust procedure for quickly localizing an impulse and for estimating its intensity from vibration measurements of a single point. The assumption is made that the impact load can be approximated as a Dirac function. The proposed technique is based on modal ponderations and general rules are provided to select the appropriate vibration modes in the analysis. Both

the accuracy and the robustness of this impulse identification technique are investigated. In particular, specific sensor locations are proposed to increase the robustness of the procedure. Experiments are conducted on a simply supported plate to demonstrate the presented method.

This paper is organized as follow. Section 2 introduces the assumptions underlying the theoretical framework and a procedure is described for estimating modal ponderations from acceleration measurements. It is proved in section 3 that modal ponderations are a robust signature of impact location if appropriate vibration modes are selected in the analysis. The proposed impulse identification procedure is then presented. Sufficient conditions are provided in section 4 for estimating the modal ponderations with accuracy and robustness. Eventually, section 5 addresses the experimental validation of the proposed impulse identification technique on a simply supported aluminum plate.

2. Estimation of modal ponderations

2.1. Impulse response

Consider a weakly damped linear elastic structure and let S be the set of all the points of its geometry that are not blocked by the boundary conditions. Assume that the structure is submitted to a transverse impact (normal to the surface) of duration $T > 0$ applied at some point $F \in S$ at time $t = 0$. Let $t \mapsto \psi(t)$ be the normalized applied load history such that $\int_0^T |\psi(t)|dt = 1$. Let $f \neq 0$ be the impulse intensity (expressed in N.s) so that the applied load history is given by $t \mapsto f\psi(t)$. Assume that $p \geq 2$ non-rigid vibration modes are known and that the structure is initially at rest (null initial conditions). The natural pulsation of the j-th mode is noted $\omega_{0j} > 0$ and its damping ratio is noted $\eta_j < 1$. The transverse vibration response $t \mapsto q(t)$ is considered at some point $C \in S$ (see Figure 1). Let's note $\phi_j(M)$ the j-th mode shape evaluated at some point $M \in S$ along the transverse direction. Assuming a modal behavior [21], the projection $\tilde{q}$ of q on the p known vibration modes is given by:

$$\tilde{q}(t) = \sum_{j=1}^{p} \phi_j(C)\phi_j(F)(f\psi * g_j)(t) \tag{1}$$

where $f\psi * g_j$ denotes the convolution product between the load history and the impulse response of the j-th modal coordinate. This latter is defined by:

$$g_j(t) = \frac{1}{\omega_j} e^{-\eta_j \omega_{0j} t} \sin(\omega_j t) \tag{2}$$

with $\omega_j = \omega_{0j}\sqrt{1-\eta_j^2}$. If the impact duration T is short enough then ψ can be modelled with a Dirac function δ. In this case, $\tilde{q}$ is well approximated at any time by:

$$\tilde{q}(t) \approx \sum_{j=1}^{p} f\phi_j(C)\phi_j(F)g_j(t) \tag{3}$$

If equation (3) holds it is said in the following that the applied impact is an impulse, relatively to the dynamics of the p vibration modes considered in the analysis.

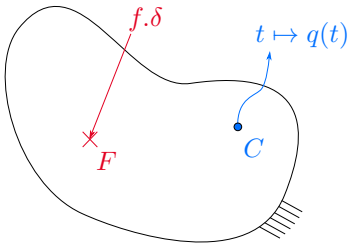

Figure 1: Dirac-like impact at point F producing a vibration response at point C.

2.2. Amplified Modal Ponderation Vector (AMPV)

Depending on impulse location F, equation (3) shows that the p vibration modes are not excited in the same proportions through the ponderations $(\phi_j(F))_{1\leq j\leq p}$. If the impulse occurs at the modal node of the i-th mode then it will not participate to the response ($\phi_i(F) = 0$). The impulse intensity f does not change the proportions in which the modes are excited: it uniformly amplifies each modal ponderation. Therefore, we introduce the Amplified Modal Ponderation Vector (AMPV) defined by $\mathbf{Z_F} = f.(\phi_1(F)\ ...\ \phi_p(F))^T$. It can be seen as the image of the impulse parameters in the vibration response: $(F, f) \mapsto \mathbf{Z_F}$. It is the purpose of section 3 to show that the reverse link $\mathbf{Z_F} \mapsto (F, f)$ holds if appropriate vibration modes are selected in the analysis.

It is straightforward to notice that the vibration response is linear with respect to the AMPV. Indeed, equation (3) can be written:

$$\tilde{q}(t) = \mathbf{L}(t).\mathbf{Z_F} \tag{4}$$

with $\mathbf{L}(t) = (\phi_1(C)g_1(t)\ ...\ \phi_p(C)g_p(t))$. The modal properties of the p selected modes are known hence $\mathbf{L}$ can be evaluated at any time. The previous equation also holds for an acceleration response model by derivating twice with respect to time:

$$\tilde{a}(t) = \ddot{\mathbf{L}}(t).\mathbf{Z_F} \tag{5}$$

In comparison with displacement sensors, accelerometers are generally smaller and do not require a reference point. Hence acceleration measurements are in practice preferred for estimating the modal ponderations.

2.3. Estimation of the AMPV

Let $(a(t_i))_{1\leq i\leq n}$ be n samples of the acceleration response at some point C of the structure. Measurements are taken at times $t_i = i\Delta t$ with Δt the sampling period of the accelerometer. A linear least-squares procedure is proposed to estimate the AMPV from data that are possibly affected by noise. The cost function J to be minimized is expressed as follows:

$$J(\mathbf{Z}) = \sum_{i=1}^{n} (\ddot{\mathbf{L}}_\mathbf{i}.\mathbf{Z} - a(t_i))^2 \tag{6}$$

where $\ddot{\mathbf{L}}_\mathbf{i} = \ddot{\mathbf{L}}(t_i)$. Equation (6) can be written in the convenient form:

$$J(\mathbf{Z}) = \mathbf{Z}^T\mathbf{A}\mathbf{Z} - 2\mathbf{U}^T\mathbf{Z} - c \tag{7}$$

with $\mathbf{A} = \sum_{i=1}^{n} \ddot{\mathbf{L}}_\mathbf{i}^T\ddot{\mathbf{L}}_\mathbf{i}$, $\mathbf{U} = \sum_{i=1}^{n} a(t_i)\ddot{\mathbf{L}}_\mathbf{i}^T$ and $c = \sum_{i=1}^{n} a(t_i)^2$. It is known that the minimum of J is unique if, and only if, the $p \times p$ matrix $\mathbf{A}$ is regular [22]. In that case, the minimum is reached for:

$$\hat{\mathbf{Z}}_\mathbf{F} = \mathbf{A}^{-1}\mathbf{U} \tag{8}$$

The regularity of the matrix $\mathbf{A}$ is a requirement for the unique estimation of the AMPV. It is the purpose of section 4 to study the properties of this matrix in order to select adequate measurement parameters (sensor location, sampling frequency and acquisition duration).

3. Reverse link between the AMPV and the impulse parameters

The purpose of this section is to prove that the identification of specific modal ponderations leads to the impulse parameters. The validity and the robustness of the reverse link $\mathbf{Z_F} \mapsto (F, f)$ are investigated. The theoretical concepts of Discriminating Modes Family (DMF) and Angular Robustness Maps (ARM) are introduced and illustrated with the experimental use-case in section 5.

3.1. Discriminating Modes Family (DMF)

Assume that the amplified modal ponderation vector $\mathbf{Z_F} \in \mathbb{R}^p$ associated to an impulse (F, f) is known. Two cases are considered:

Case 1: $\mathbf{Z_F} = \mathbf{0}$. Each modal ponderation is null, hence the impact occurred at an intersection point of the nodal lines of the modes kept in the analysis. Let's note $L_j(0) = \{M \in S \mid \phi_j(M) = 0\}$ the j-th nodal line. Then:

$$F \in \cap_{j=1}^{p} L_j(0) \tag{9}$$

Case 2: $\mathbf{Z_F} \neq \mathbf{0}$. At least one of the modal ponderations is not null, say $\phi_i(F) \neq 0$. One can write:

$$\mathbf{Z_F} \propto \left(\frac{\phi_1}{\phi_i}(F) \ ... \ \frac{\phi_{i-1}}{\phi_i}(F) \ 1 \ \frac{\phi_{i+1}}{\phi_i}(F) \ ... \ \frac{\phi_p}{\phi_i}(F) \right)^T \tag{10}$$

At this step, the idea is to extend the previous concept of nodal line to the concept of iso-proportion line between two vibration modes. More precisely, let's define $L_{j/i}(\alpha) = \{M \in S \mid \phi_j(M) = \alpha\phi_i(M)\}$ with α a real number. Then, similarly to the previous case, the impact occurred at an intersection point of $p-1$ iso-proportion lines:

$$F \in \cap_{j=1, j\neq i}^{p} L_{j/i}(\lambda_{ji}) \tag{11}$$

with $\lambda_{ji} = \phi_j(F)/\phi_i(F)$. Note that all the coefficients λ_{ji} are known since the AMPV is assumed known.

The previous discussion suggests to introduce the following set of points:

$$I(F) = \begin{cases} \cap_{j=1}^{p} L_j(0) & \text{if } \phi_j(F) = 0 \text{ for any } j \in [\![1, p]\!] \\ \cap_{j=1, j\neq i}^{p} L_{j/i}(\lambda_{ji}) & \text{if } \phi_i(F) \neq 0 \text{ for some } i \in [\![1, p]\!] \end{cases} \tag{12}$$

It becomes clear that the AMPV is bijectively linked to the impulse location if, and only if:

$$I(F) = \{F\} \tag{13}$$

In this case, it is said that $\mathcal{F} = (\phi_j)_{1 \leq j \leq p}$ is a Discriminating Modes Family (DMF) for the point $F \in S$. If this unique intersection point property holds for any $M \in S$, then it is said that $\mathcal{F}$ is a global DMF of the structure. An example of a global DMF is given in section 5.2.1.

It must be mentioned at this stage that the identification of a DMF from a known family of vibration modes is a combinatory problem. A tool is however presented in section 3.3 to help identifying and selecting one.

3.2. Truncation of the modal matrix on a global DMF

In practice, mode shapes are often not analytically known, hence iso-proportion lines cannot be used to determine the impulse location. The structure is generally discretized to evaluate, either experimentally or numerically, the mode shapes at several Degrees Of Freedom (DOF). Let $\phi_{\mathbf{i}} \in \mathbb{R}^N$ be the i-th discretized mode shape evaluated along N transverse DOFs. Then the $N \times p$ modal matrix $\mathbf{\Phi} = [\phi_{\mathbf{1}}|...|\phi_{\mathbf{p}}]$ is available. The columns of its transpose are noted $\phi^*_{\mathbf{i}} \in \mathbb{R}^p$ so that:

$$\mathbf{\Phi}^T = [\phi^*_{\mathbf{1}}|...|\phi^*_{\mathbf{N}}] \tag{14}$$

To simplify the notations, let's abusively note $F \in [\![1, N]\!]$ the index of the DOF at which an impulse of intensity f occurred. Then the AMPV is given by:

$$\mathbf{Z_F} = f\phi^*_{\mathbf{F}} \tag{15}$$

It is a remarkable property that if the modal matrix is truncated on a global DMF, then for any $i \neq j$ the couple $(\phi^*_{\mathbf{i}}, \phi^*_{\mathbf{j}})$ is independent [23]. In other words, each DOF keeps its individuality in terms of modal ponderations if discriminating vibration modes are selected in the analysis. In particular, this property provides the basic idea of the proposed impulse identification technique (presented in its final form in section 3.4):

- The impulse location $F \in S$ corresponds to the unique index $i \in [\![1, N]\!]$ such that $\mathbf{Z_F}$ and $\phi^*_{\mathbf{i}}$ are collinear,
- The impulse intensity f is the collinearity factor between $\mathbf{Z_F}$ and $\phi^*_{\mathbf{i}}$.

It can be appreciated that the nonlinear inverse problem of impulse localization is replaced by the linear inverse problem (8) followed by a simple collinearity research procedure. However the estimated AMPV $\hat{\mathbf{Z}}_{\mathbf{F}}$ might not be exactly collinear to a column of $\mathbf{\Phi^T}$. More theory is presented in next section to adapt the above-mentioned technique to real cases.

3.3. Angular Robustness Map (ARM)

In practice the AMPV is always affected by an estimation error:

$$\hat{\mathbf{Z}}_{\mathbf{F}} = \mathbf{Z_F} + \mathbf{e} \tag{16}$$

The error term $\mathbf{e} \in \mathbb{R}^p$ may be due to some noise contiminating the data, due to modelling errors in (3), or due to the fact that the impact occurred at a DOF at which the mode shapes have not been evaluated. Consequently $\hat{\mathbf{Z}}_{\mathbf{F}}$ might not be exactly collinear to a column of $\mathbf{\Phi^T}$. Instead we shall look for the columns of $\mathbf{\Phi}^T$ that are roughly collinear to $\hat{\mathbf{Z}}_{\mathbf{F}}$. This can be done by introducing a collinearity tolerance in the procedure. In the following, the angle between two vectors $\mathbf{u}$ and $\mathbf{v}$ is defined by the small angle $\theta \in [0, \pi/2]$ between $\mathbf{v}$ and span $(\mathbf{u})$ (see Figure 2).

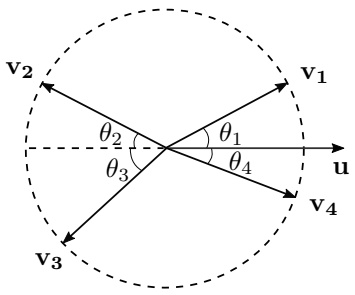

Figure 2: Definition of the small angles between a vector $\mathbf{u}$ and other vectors $\mathbf{v_i}$.

Let's note $\epsilon > 0$ a proximity tolerance as an objective of localization performance. For instance, in the use-case presented in section 5 the objective is to localize all the applied impacts within 3.6cm. A collinearity tolerance angle θ_c is said admissible (for the proximity tolerance ϵ and for the impact point F) if all the $\phi_{\mathbf{i}}^*$ making a small angle with $\phi_{\mathbf{F}}^*$ lower or equal than θ_c are associated to points $F_i \in S$ such that $\|F_i - F\| \leq \epsilon$.

Now let's introduce $\theta_\epsilon(F)$ as the maximum admissible collinearity tolerance for the proximity tolerance ϵ and for the impact point F. Figure 4 presents a procedure for evaluating θ_ϵ at the N DOFs of the structure. It becomes straightforward to notice (see Figure 3) that all the candidates F_i are within the proximity tolerance ϵ if the following condition is satisfied:

$$\theta_c + \hat{\theta}_F < \theta_\epsilon(F) \tag{17}$$

where $\hat{\theta}_F$ is the small angle (unknown in practice) between $\hat{\mathbf{Z}}_{\mathbf{F}}$ and $\phi_{\mathbf{F}}^*$.

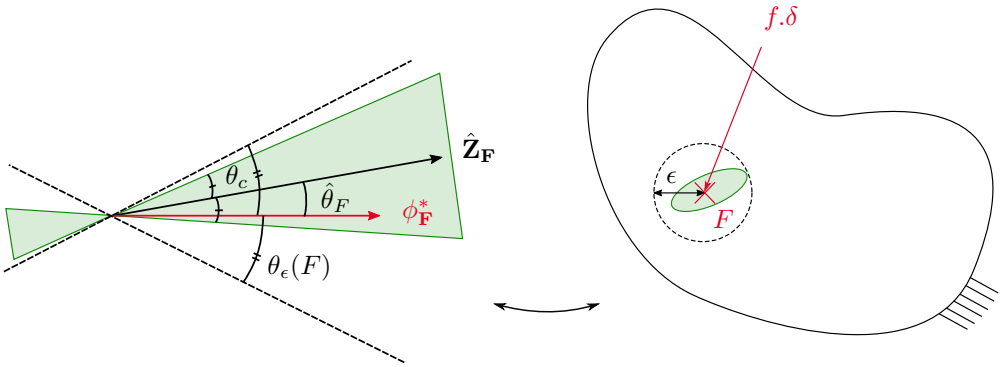

Figure 3: Conversion of the proximity tolerance ϵ into a collinearity tolerance $\theta_\epsilon(F)$.

Finally, for a given proximity tolerance ϵ, we define for a given vibration modes family its Angular Robustness Map (ARM) by the mapping:

$$M \mapsto \theta_\epsilon(M) \tag{18}$$

The ARM is an important tool to determine if a given vibration modes family is suitable for localizing impacts within a desired proximity tolerance. If θ_ϵ is null in an area of the structure then the ϵ-localization of any impact applied in this area will fail. On the other hand, higher values of θ_ϵ in an area of the structure mean that the procedure can resist larger estimation errors on the AMPV. Several ARMs are presented in section 5.2.2.

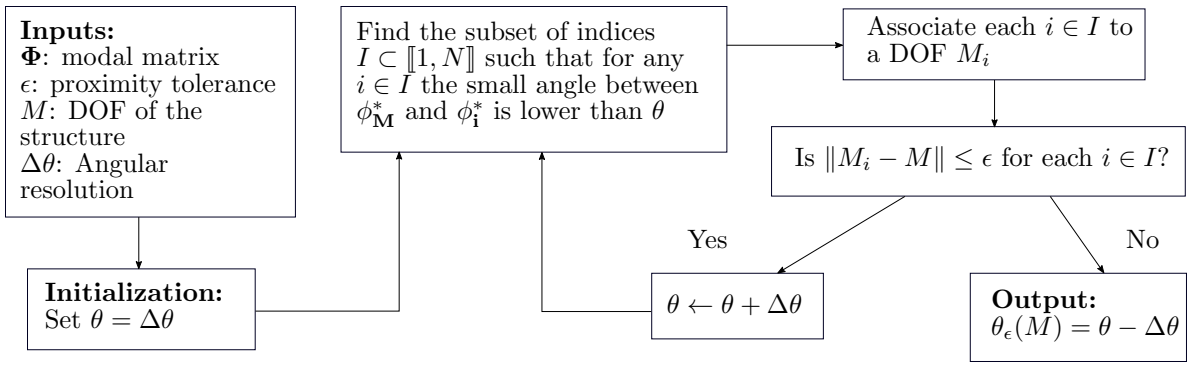

Figure 4: Procedure to evaluate $\theta_\epsilon(M)$.

3.4. Impulse identification technique with an adaptive collinearity tolerance

As discussed in previous section there might be important discrepancies in the values of θ_ϵ. Therefore it is proposed to use an adaptive collinearity tolerance in the procedure as follow. First let's arbitrarily chose a fixed collinearity tolerance $\theta_c \in]0, \pi/4]$ to consider only candidates $F_i \in S$ associated to $\phi_{\mathbf{i}}^*$ making a relatively small angle with $\hat{\mathbf{Z}}_{\mathbf{F}}$. Then let's chose a dispersion factor $\gamma \geq 1$ to reject candidates associated to the largest angles. The impulse identification technique with an adaptive collinearity tolerance is then:

Inputs: Acceleration measurements, modal matrix $\mathbf{\Phi}$ truncated on a DMF, collinearity tolerance θ_c, dispersion factor γ

Step 1: Estimate the AMPV $\hat{\mathbf{Z}}_{\mathbf{F}}$ from the measurements with equation (8),

Step 2: Search for the subset of indices $I \subset [\![1, N]\!]$ such that for any $i \in I$ the small angle $\hat{\theta}_i$ between $\hat{\mathbf{Z}}_{\mathbf{F}}$ and $\phi_{\mathbf{i}}^*$ is lower than θ_c,

Step 3: Compute $\hat{\theta}_m = \min_i \hat{\theta}_i$ and reject all the candidates such that $\hat{\theta}_i > \gamma \hat{\theta}_m$. Update I.

Step 4: Associate each $i \in I$ to a point $F_i \in S$ and compute the collinearity factors f_i between $\hat{\mathbf{Z}}_{\mathbf{F}}$ and the $\phi_{\mathbf{i}}^*$:

$$f_i = \frac{(\phi_{\mathbf{i}}^*)^T . \hat{\mathbf{Z}}_{\mathbf{F}}}{\|\phi_{\mathbf{i}}^*\|_2^2} \tag{19}$$

Step 5: Estimate the impulse intensity with a weighted barycenter:

$$\hat{f} = \sum_{i \in I} w_i f_i \tag{20}$$

with $w_i \geq 0$ and $\sum_{i \in I} w_i = 1$. In this study $w_i = \cos(\hat{\theta}_i) / \sum_{k \in I} \cos(\hat{\theta}_k)$ to give more weight to candidates associated to small $\hat{\theta}_i$.

Step 6: (optional) If the structure is planar within the area delimited by the candidates $F_i \in S$ then estimate the impulse location with the same formula:

$$\hat{F} = \sum_{i \in I} w_i F_i \tag{21}$$

Outputs: Estimation of the impulse intensity $\hat{f}$ and location $\hat{F}$

Note that the sensivity of γ on the localization results is low if $\hat{\theta}_m \approx 0$. Note also that $\gamma = 1$ consists in selecting the candidate (provided it is unique) associated to the $\phi_{\mathbf{i}}^*$ the most collinear to $\hat{\mathbf{Z}}_{\mathbf{F}}$. However it has been observed in [23] that moderate values of γ, between 2 and 10, provide the most accurate and robust results. No rule has however been found yet to select an optimal value of γ prior testing the technique on several impacts.

3.5. Implementation

Figure 5 illustrates the program flowchart of the proposed impulse identification technique. Several steps of the procedure are described in the following:

DMF identification. This is a combinatory problem to be solved, with trials and errors, by plotting the ARMs of several modes families associated to a desired proximity tolerance ϵ. As a rule of thumb the minimum value of θ_ϵ should be greater than 3-4°in the area of the structure submitted to impacts. From [23], if d is the dimensionality of the structure's geometry (e.g. $d = 2$ for a plate) then the minimum number of modes to be kept in the analysis to form a DMF is $p_{min} = d + 1$. Hence only combinations of at least $d + 1$ modes should be considered for plotting the ARMs (e.g. $p = 3$ for a plate).

Measurement parameters. Once a DMF is identified, the sampling frequency and the acquisition duration should be selected, as a rule of thumb, such that:

$$\Delta t \leq \frac{2\pi}{10 \times \omega_{0p}}, \quad D \geq 10 \times \frac{2\pi}{\omega_{01}} \tag{22}$$

where ω_{01} and ω_{0p} are respectively the lowest and the highest natural pulsations of the modes in the selected DMF. The dynamics of the vibration modes selected for the analysis can then be correctly captured.

Sensor location. The sensor can be positionned on a point C such that the condition number in 2-norm $\kappa_a(\mathbf{A}, C)$ of the matrix $\mathbf{A}$ defined in section 2.3 is minimal (see example in section 5.2.3). The robustness of the inversion (8) is then increased.

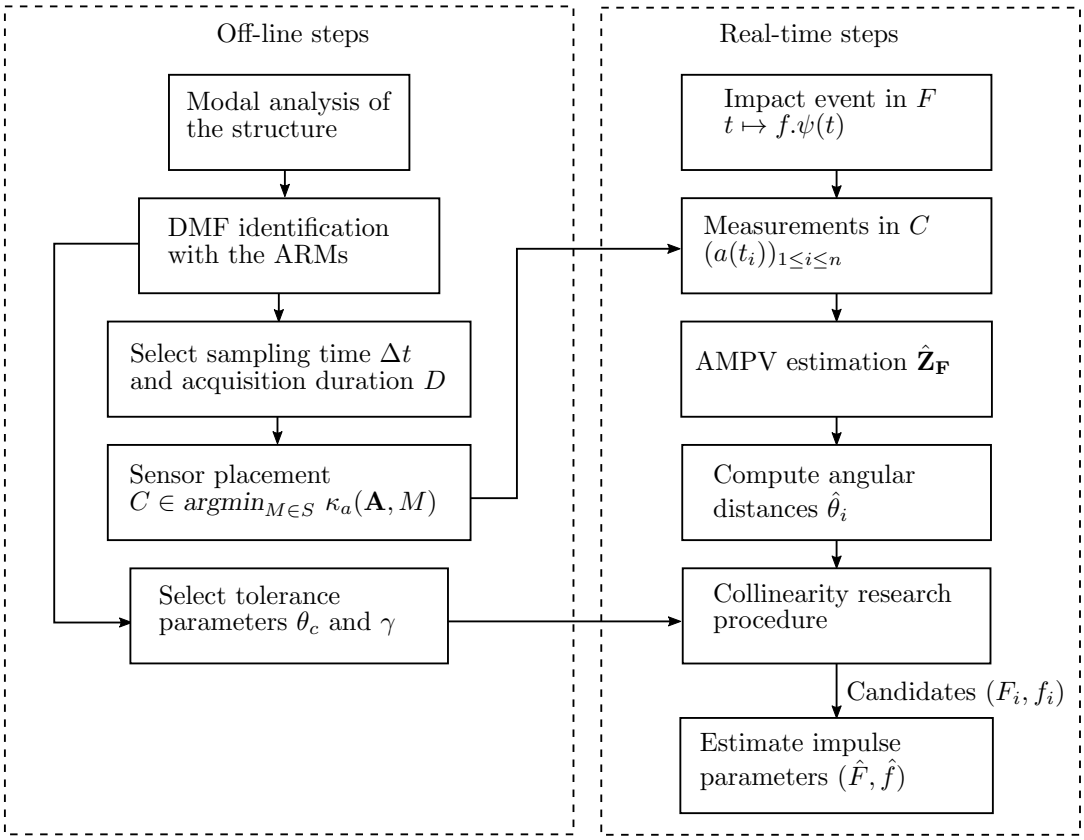

Figure 5: Program flowchart of the impulse identification technique.

4. Conditions for an accurate and robust impulse localization

Accuracy and robustness are desirable properties for an impact localization technique. For instance, consider the localization results of numerous impacts applied at the same point F of a plate-like structure. Each repetition is somehow different, which traduces in different perturbations of the model response (3). The technique is said accurate for localizing an impact applied in F if the center of the estimates $(\hat{F}_i)$ is near F ; it is said robust if the diameter of the set of all the estimates $(\hat{F}_i)$ is small. Figure 6 shows that a localization technique can be inaccurate but robust, or accurate but not robust.

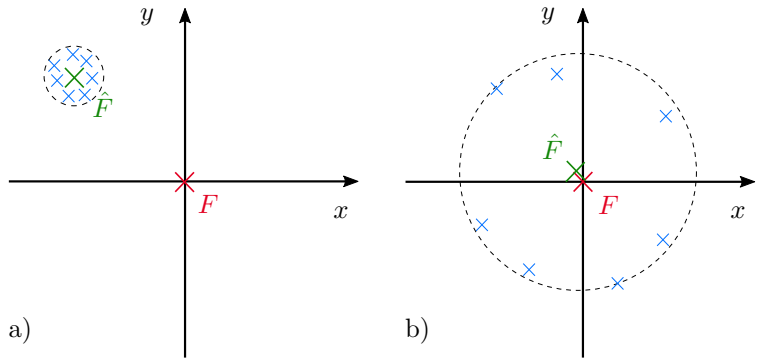

Figure 6: The localization technique is a) inaccurate but robust b) accurate but not robust.

The objective of this section is to propose sufficient conditions for an accurate and robust estimation of the AMPV. Displacement measurements are considered in the following to simplify mathematical expressions. These latter can be adapted to acceleration measurements by noticing that $\ddot{g}_i$ takes the form:

$$\ddot{g}_i(t) = -\frac{\omega_{0i}^2}{\sqrt{1-\eta_i^2}} g_i(t+\tau_i) \tag{23}$$

The proofs of the important relations are given in the Appendix to enhance the readability.

4.1. Almost-orthogonality conditions (a-o conditions)

The general term of matrix $\mathbf{A}$, defined in section 2.3, is given by:

$$A_{ij} = \phi_i(C)\phi_j(C).\left(\mathbf{G_i}^T.\mathbf{G_j}\right) \tag{24}$$

where $\mathbf{G_i} = (g_i(t_1)\ ...\ g_i(t_n))^T$ is the i-th modal impulse response discretized in time. Let's define the modal separation s_{ij} between two modes i and j by a real number within 0 and 1:

$$s_{ij} = \frac{|\omega_{0i} - \omega_{0j}|}{\omega_i + \omega_j} \tag{25}$$

If the sampling frequency and the acquisition duration are large enough, then the normalized elements $\mathbf{G_i^*} = \mathbf{G_i}/\|\mathbf{G_i}\|$ satisfy (see Appendix):

$$\|\mathbf{G_i^*}\| = 1 \qquad \text{and for } i \neq j \qquad |(\mathbf{G_i^*})^T.\mathbf{G_j^*}| \leq \mu_p = \frac{\mu + \eta_{Max}^2}{1-\eta_{Max}^2} \tag{26}$$

with:

$$\mu = \frac{\eta_{Max}^2}{(1-(\eta_{Max}^2-\eta_{min}^2))(\eta_{min}^2+s^2)} \tag{27}$$

$$\eta_{min} = \min_i \eta_i \tag{28}$$

$$\eta_{Max} = \max_i \eta_i \tag{29}$$

$$s = \min_{i \neq j} s_{ij} \tag{30}$$

If the p vibration modes selected in the analysis are weakly damped (η_{Max} is small) and well separated (s is high), then the normalized family $(\mathbf{G_i^*})_{1 \leq i \leq p}$ is almost-orthogonal (a-o):

$$\mu_p \ll 1 \tag{31}$$

This can be understood by the fact that $\mathbf{G_i}^T.\mathbf{G_j}$ is similar to an integral of harmonic functions if modal dampings are small, natural frequencies are separated, and both sampling frequency and observation duration are large enough. Note that a-o conditions have a practical meaning only if the smallnest of the a-o coefficient μ_p is specified (see sections 4.2 and 4.3).

4.2. Accuracy with a modal truncation error

Let $\mathbf{Q}$ be the discretized measured response and assume that $\mathbf{Q}$ has a decomposition in a family of $m > p$ discretized modal impulse responses $(\mathbf{G_i})_{1 \leq i \leq m}$. Let $\tilde{\mathbf{Q}}$ be the discretized model response (3). Let's note $\mathbf{Q_e} = \mathbf{Q} - \tilde{\mathbf{Q}}$ the modelization error. This latter may be due to the modal truncation as only p vibration modes are kept in the analysis, while $m > p$ vibrations modes are significantly excited. The accuracy of the AMPV estimation, the modelization error and the a-o coefficient are linked as follow:

$$\|\hat{\mathbf{Z}}_\mathbf{F} - \mathbf{Z_F}\|_\infty \leq c.\mu_m.(m-p)\|\mathbf{Q_e}\|_\infty \tag{32}$$

where μ_m is the a-o coefficient of the family $(\mathbf{G_i^*})_{1 \leq i \leq m}$ obtained by evaluating equation (27) with the corresponding family of m modes, and where c is a constant independent of m.

The relation (32) shows that the truncation error term, included in $(m-p)\|\mathbf{Q_e}\|_\infty$, can be attenuated by the almost-orthogonality of the modal impulse responses. Hence the AMPV can be accurately estimated in a-o conditions, even if the modal truncation error is important.

4.3. Robustness with appropriate sensor placement

A necessary condition for the sensor position is to avoid the nodal lines of the p modes selected in the analysis:

$$C \notin \cup_{i=1}^{p} L_i(0) \tag{33}$$

Otherwise the matrix $\mathbf{A}$ is singular. From a physical point of view, if $C \in L_k(0)$ then the ponderation of mode k, namely $\phi_k(F)$, is not sensed hence it cannot be estimated.

If relation (33) holds and if μ_p is small enough, then it is a remarkable property that the matrix $\mathbf{A}$ takes a strictly dominant diagonal form:

$$|A_{ii}| > \sum_{j \neq i}^{p} |A_{ij}| \tag{34}$$

From [24], the condition number in 2-norm of such a matrix can be approximated by the largest ratio of its diagonal coefficients:

$$\kappa_d(\mathbf{A}, C) \approx \max\left(\frac{\phi_j^2(C)}{\eta_j \omega_{0j}^3}\right) / \min\left(\frac{\phi_j^2(C)}{\eta_j \omega_{0j}^3}\right) \tag{35}$$

where the underscript "d" in κ_d refers to displacement measurements. In practice, acceleration measurements are used (see section 2.3). It can be proved [23] in a similar manner that:

$$\kappa_a(\mathbf{A}, C) \approx \max\left(\frac{\omega_{0j}\phi_j^2(C)}{\eta_j}\right) / \min\left(\frac{\omega_{0j}\phi_j^2(C)}{\eta_j}\right) \tag{36}$$

This approximation is discussed in section 5.4. One can minimize the condition number of $\mathbf{A}$ by adequatly positioning the sensor on a robustness point:

$$C \in \mathit{argmin}_{M \in S}\ \kappa_a(\mathbf{A}, M) \tag{37}$$

In particular, if relation (33) is not satisfied then $\kappa_a(\mathbf{A}, C) = +\infty$, hence the matrix $\mathbf{A}$ is singular.

4.4. Summary

The AMPV estimation is accurate and robust if the following conditions are satisfied:

(i) The vibration modes significantly excited by the impact are weakly damped and well separated,

(ii) The sampling frequency and the acquisition duration are large enough,

(iii) The sensor is not located near a modal node of one of the p modes selected in the analysis.

It is important to notice that condition (i) depends on the modal properties of the structure, while conditions (ii)-(iii) depend on the measurement parameters.

5. Experimental validation on a simply supported metallic plate

The purpose of this section is to validate the proposed single-sensor approach for impulse identification. Experimental studies are conducted on an academic structure in order to ease the modal analysis step (see Figure 5) and to illustrate the new concepts introduced in previous sections.

5.1. Set-up

The experimental set-up consists in a rectangular aluminum plate mounted on a specific support that reproduces simply supported boundary conditions (see Figure 7). The details of this set-up are described in [25]. Plate properties are given in Table 1. A Finite Element Model (FEM) of the plate is created with Nastran 2014 to compute the first six mode shapes of the plate. The FEM consists in a plate discretized in 8×8 CQUAD8 elements. Hence the plate is divided in 64 rectangular cells of dimension $a_e \times b_e$ with $a_e = 4.5$cm and $b_e = 5.25$cm. This grid allows a spatial resolution for the localization problem of $\min(a_e/2, b_e/2) = 2.25$ cm. The number of unblocked DOFs in the transverse direction of the plate is $N = 161$.

Three accelerometers 352C22 PCB Piezotronics are glued to the surface of the plate at points $C_1 = (3a_e, 3b_e)$, $C_2 = (6a_e, 5b_e)$ and $C_3 = (2a_e, 6b_e)$ (see section 5.2.3). Impacts are applied with the steel tip of an impact hammer IH-02 Tenlee Piezotronics. Impact load history and acceleration data are recorded with the software m+p Analyzer Rev 5.1 with a sampling frequency of 12.8kHz and a total measurement duration of 0.64s.

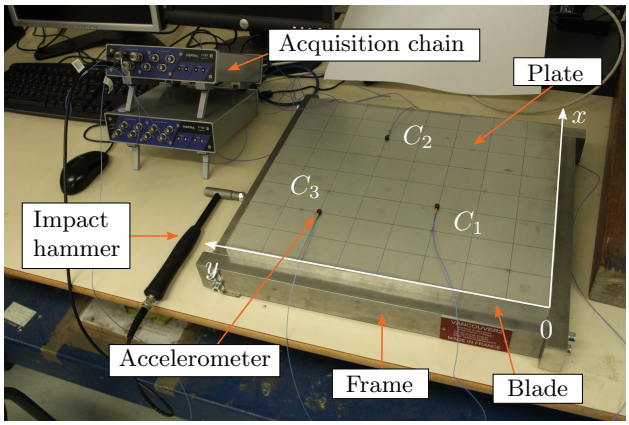

Figure 7: Experimental set-up.

Dimensions	$a = 36$cm, $b = 42$cm, $h = 3$mm
Density	2800 kg.m^{-3}
Young modulus	72.5 GPa
Poisson ratio	0.33
Mode 1	$\omega_{01} = 595$ rad/s, $\eta_1 = 1\%$
Mode 2	$\omega_{02} = 1406$ rad/s, $\eta_2 = 0.3\%$
Mode 3	$\omega_{03} = 1693$ rad/s, $\eta_3 = 0.6\%$
Mode 4	$\omega_{04} = 2454$ rad/s, $\eta_4 = 0.3\%$
Mode 5	$\omega_{05} = 2700$ rad/s, $\eta_5 = 0.09\%$
Mode 6	$\omega_{06} = 3438$ rad/s, $\eta_6 = 0.14\%$

Table 1: Properties of the plate manufactured by Vancouver2 (Toulouse, France) and results of an experimental modal analysis.

5.2. Theoretical predictions

5.2.1. Global DMF

From [26], the (i,j) mass-normalized flexural mode shape of a simply supported plate is given by:

$$\phi_{i,j}(x,y) \propto \sin\left(\frac{i\pi x}{a}\right)\sin\left(\frac{j\pi y}{b}\right) \tag{38}$$

Let's note $\phi_1 = \phi_{1,1}, \phi_2 = \phi_{1,2}$, and $\phi_3 = \phi_{2,1}$. The objective is to show that $\mathcal{F}_1 = (\phi_1, \phi_2, \phi_3)$ is a global DMF of the plate (see Figure 8).

Let $S =]0,a[\times]0,b[$ be the set of all the points of the plate that are not blocked by boundary conditions. Let $F = (x_F \ y_F) \in S$ be a point of the plate submitted to a transverse impulse with an arbitrary intensity $f \neq 0$. The first mode is necessarily excited: $\phi_1(F) \neq 0$. The associated AMPV can be normalized as follow:

$$\mathbf{Z_F} \propto \left(1 \ \frac{\phi_2}{\phi_1}(F) \ \frac{\phi_3}{\phi_1}(F)\right)^T = (1 \ \lambda_{21} \ \lambda_{31})^T \tag{39}$$

with $\lambda_{21} = \sin\left(\frac{2\pi y_F}{b}\right) / \sin\left(\frac{\pi y_F}{b}\right)$ and $\lambda_{31} = \sin\left(\frac{2\pi x_F}{a}\right) / \sin\left(\frac{\pi x_F}{a}\right)$. By using mode shape equation (38) and the notations of section 3.1, it is straightforward to show:

$$L_{2/1}(\lambda_{21}) = \{(x,y) \in S \mid y = y_F\} \tag{40}$$
$$L_{3/1}(\lambda_{31}) = \{(x,y) \in S \mid x = x_F\} \tag{41}$$

Thus $I(F) = \{F\}$ for any $F \in S$. Therefore, $\mathcal{F}_1$ is a global DMF of the plate. Intuitively, ϕ_1 acts as a non uniform reference, ϕ_2 allows to discriminate upper/lower halves of the plate, and ϕ_3 allows to discriminate right/left halves.

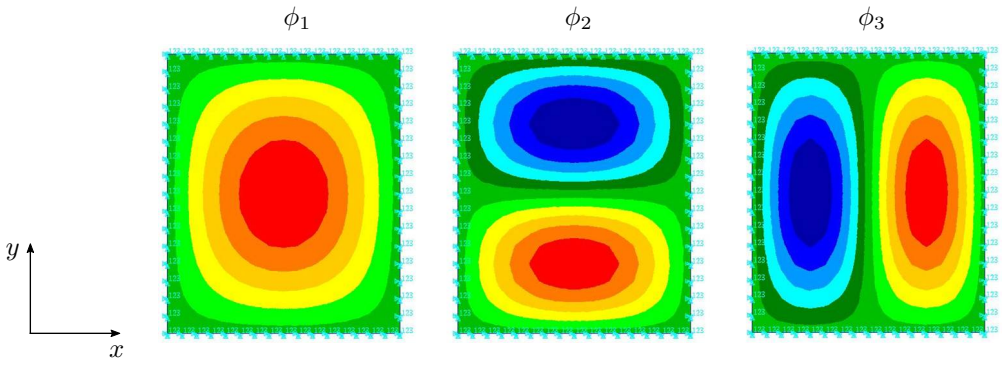

Figure 8: Mode shapes of the global DMF $\mathcal{F}_1 = (\phi_1, \phi_2, \phi_3)$.

5.2.2. Angular Robustness Maps (ARMs)

The modal truncation error may be too large for accurately estimating the AMPV if only the three vibration modes of $\mathcal{F}_1$ are kept in the analysis (see section 4.2). However, it is straightforward to notice that adding a mode to a DMF forms a new DMF. The idea is then to iteratively add one mode to $\mathcal{F}_1$ in order to improve the ARMs (see section 3.3). This process successively leads to $\mathcal{F}_2 = (\mathcal{F}_1, \phi_5)$, $\mathcal{F}_3 = (\mathcal{F}_2, \phi_6)$ and eventually $\mathcal{F}_4 = (\mathcal{F}_3, \phi_4)$. Figure 9 shows the ARMs of these different modes families with $\epsilon = 3.63$cm (see section 5.3.1). It can be seen that successively adding appropriate modes in the analysis increases both minimal and maximal values of θ_ϵ. These maps are used in section 5.3.2 to interpret the localization results.

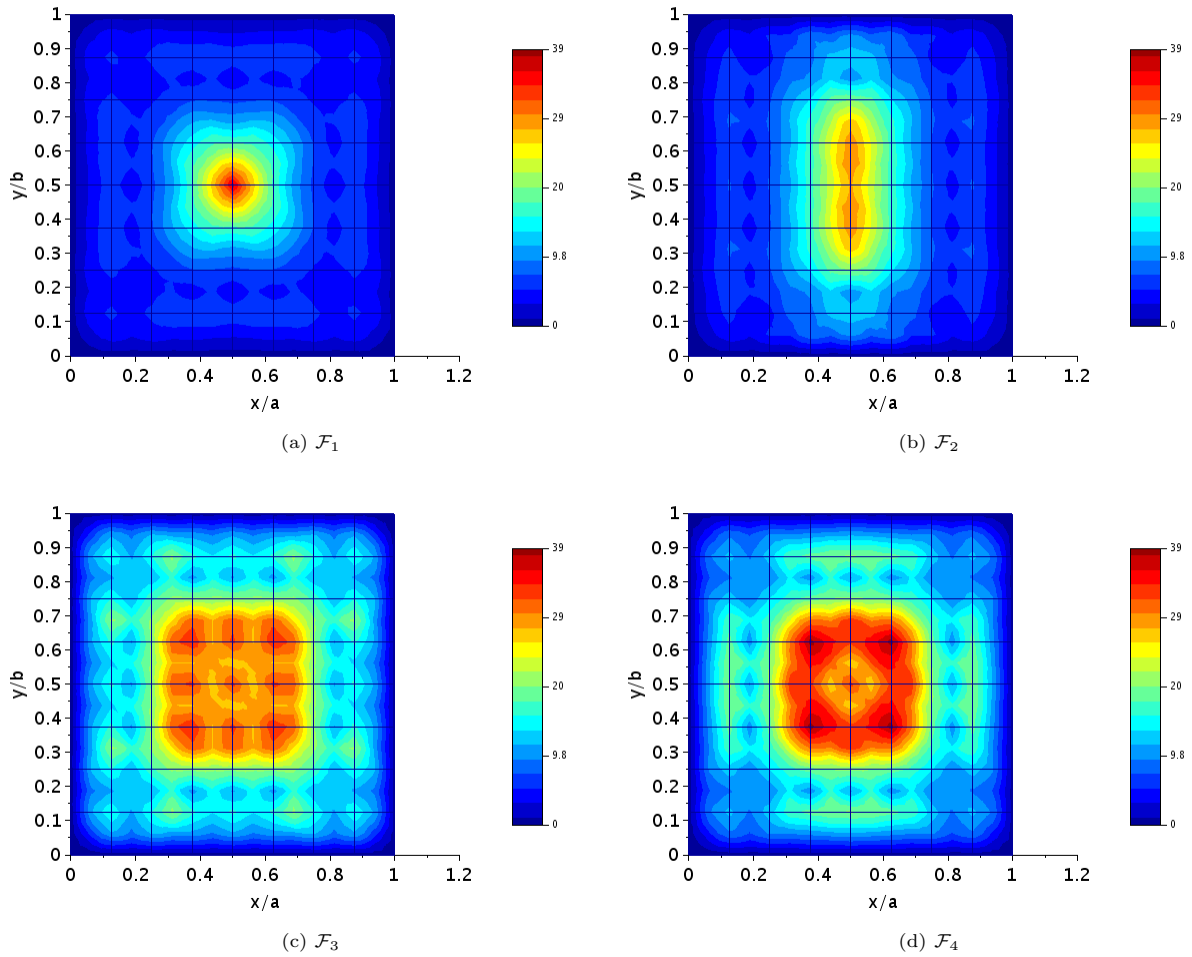

(a) $\mathcal{F}_1$ (b) $\mathcal{F}_2$

(c) $\mathcal{F}_3$ (d) $\mathcal{F}_4$

Figure 9: Angular Robustness Map $M \mapsto \theta_\epsilon(M)$ (in °) depending on modes selection (computed with $\epsilon = 3.63cm$ and $\Delta\theta = 0.1°$).

5.2.3. Identification of robustness points

The robustness of the AMPV estimation can be increased by adequatly positioning the sensor on the structure (see section 4.3). Figure 10 shows the robustness points of the plate, defined by relation (37), with the four vibration modes families. Measurement points C_1 and C_2 are robustness points of the plate (red areas), and C_3 is at the border of the robustness point areas. The three accelerometers are located at these points to validate the single-sensor approach (see Figure 7).

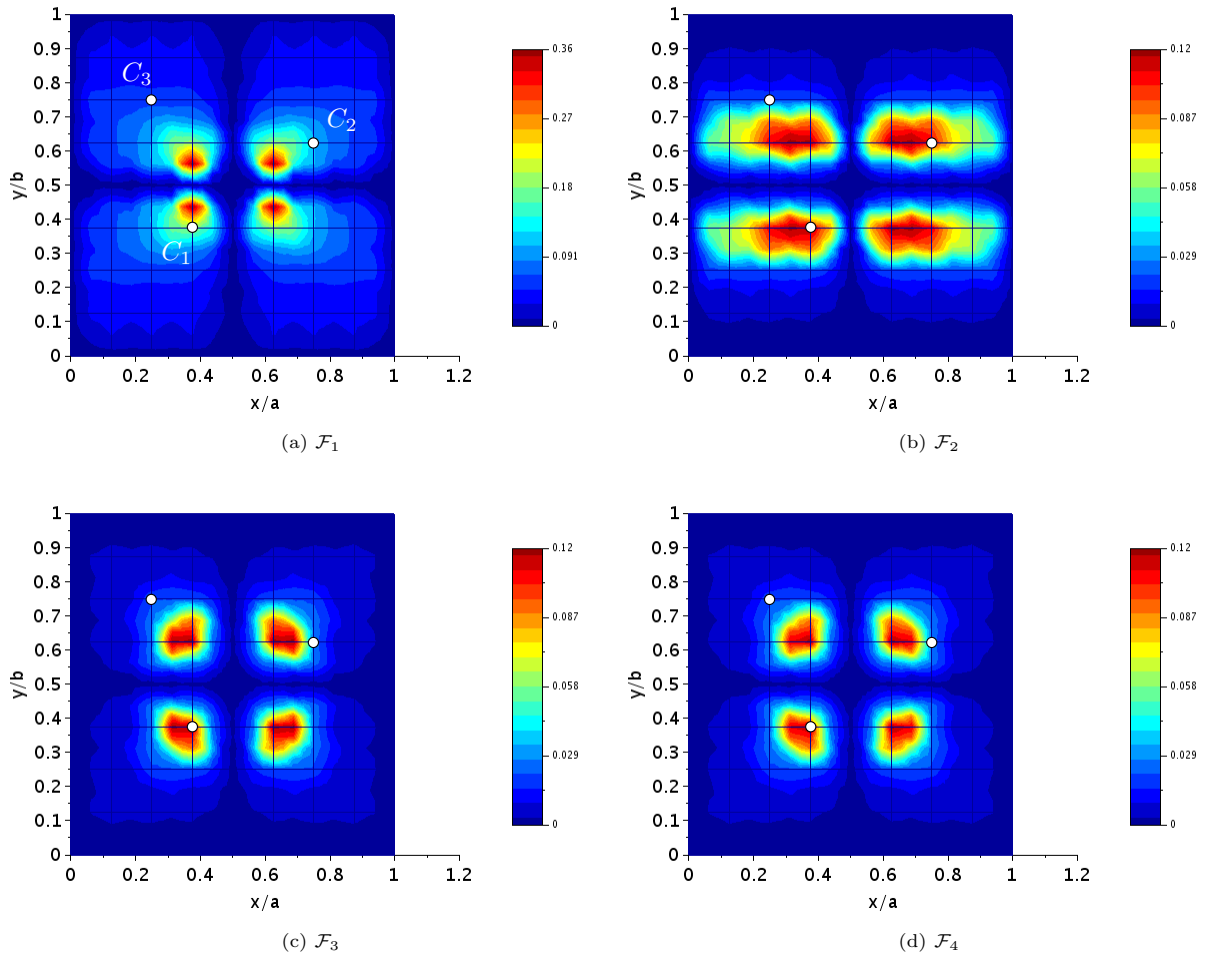

(a) $\mathcal{F}_1$ (b) $\mathcal{F}_2$

(c) $\mathcal{F}_3$ (d) $\mathcal{F}_4$

Figure 10: Points of the plate maximizing $1/\kappa(\mathbf{A})$ depending on modes selection.

5.3. Impulse identification performances

5.3.1. Description of the procedure

Impacts are applied at the center of the grid cells that are represented on Figure 7. The plate is initially at rest before each impact. The proximity tolerance is set to $\epsilon = 3.63$cm (5% more than the half of a cell diagonal). Therefore, an impact localization is considered successful if $\|\hat{F} - F\| \leq \epsilon$.

It is assumed in section 2 that the instant of impact $t = t_0$ is known ($t_0 = 0$). In practice, measurements start before the impact time hence t_0 is an unknown parameter. Consequently, the impulse identification technique is slightly modified as follow to estimate the instant of impact. The cost function (6) to be minimized becomes $J = J(\mathbf{Z}, \tau)$, where τ represents the impulse delay. A first estimation τ_0 is obtained with a threshold technique based on a level of 5% of measured acceleration amplitude: $\tau_0 = \text{argmin}|a(t_i)| > 0.05 \times \max|a(t_i)|$. Then an interval $[\tau_m, \tau_M]$ is uniformly discretized with a resolution $\Delta\tau$. The least-squares procedure described in section 2.3 is repeated for each $\tau_k = \tau_0 + k\Delta\tau$ (k may be negative). The parameter τ^* that leads to the minimal value of J is selected as the impact time:

$$t_0 = \tau^* \tag{42}$$

The parameters of the procedure are summarized in Table 2.

Cells dimensions	$a_e = 4.5$cm, $b_e = 5.25$cm
Proximity tolerance	$\epsilon = 3.6$cm
Measurement duration	$D = 10 \times \frac{2\pi}{\omega_{01}} = 0.105$s
Sampling frequency	$f_e = 1/\Delta t = 12.8kHz$
Accelerometer positions	$C_1 = (3a_e, 3b_e)$, $C_2 = (6a_e, 5b_e)$, $C_3 = (2a_e, 6b_e)$
Available modes	$(\phi_1, ..., \phi_6)$
Collinearity tolerance	$\theta_c = \pi/6$
Dispersion factor	$\gamma = 2$
Impact time estimation	$\Delta\tau = \Delta t$, $\tau_m = -5\Delta\tau$, $\tau_M = +30\Delta\tau$

Table 2: Parameters for the impulse identification procedure.

5.3.2. Localization results

Table 3 summarizes the localization performances depending on the measurement point and the DMF selection. The rate of ϵ-localization success ranges typically from 80% with $\mathcal{F}_1$ to 100% with $\mathcal{F}_4$. There is only one impact that seems more accurately localized with $\mathcal{F}_3$ than with $\mathcal{F}_4$. Perhaps the corresponding cell has not been exactly impacted at its center during the tests. The proposed single-sensor approach is however validated for accurately localizing impacts applied on a plate.

DMF	C_1	C_2	C_3
$\mathcal{F}_1$	53	52	52
$\mathcal{F}_2$	59	59	62
$\mathcal{F}_3$	64(100%)	61	63
$\mathcal{F}_4$	63	64(100%)	64(100%)

Table 3: Number of ϵ-localizations (/64) depending on accelerometer location and DMF selection.

Figure 11 shows the localization maps obtained with the accelerometer located in C_3 depending on DMF selection. Most of the impacts are successfuly localized. However, impacts applied near the borders/corners of the plate are uncorrectly localized by using $\mathcal{F}_1$. It can be seen on Figure 9a that θ_ϵ is much smaller at the borders of the plate and especially at its corners. As a result, the procedure is less robust for impacts applied at these points.

It is observed in Figures 11a and 11c that some estimates, corresponding to impacts applied near a border, are diametrically opposed to the true impact point. It happens when the estimated AMPV takes the form $\hat{\mathbf{Z}}_\mathbf{F} = (\delta \ * \ *)^T$, with δ small with respect to other coordinates. The localization error can then be explained by the symmetry of the mode shapes as follow. From Figure 12, the plate can be divided in four quadrants defined by the relative signs of the mode shapes: $Q_1 = (+,+,+), Q_2 = (+,-,+), Q_3 = (+,-,-)$ and $Q_4 = (+,+,-)$. When the first coordinate of the estimated AMPV is small with respect to the others, there is no much difference between $(\delta \ * \ *)^T$ and $(-\delta \ * \ *)^T$. As a result, the collinearity research procedure is likely to capture candidates that belong to the wrong quadrant.

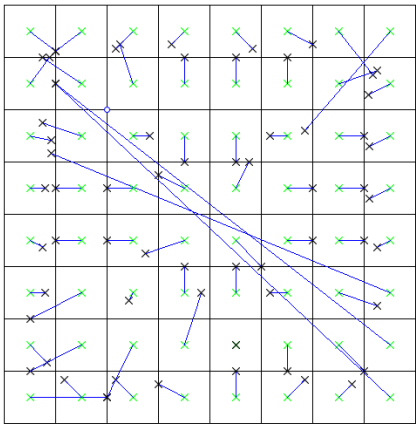

(a) $\mathcal{F}_1$

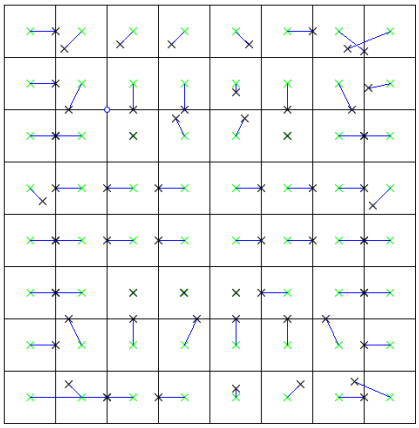

(b) $\mathcal{F}_2$

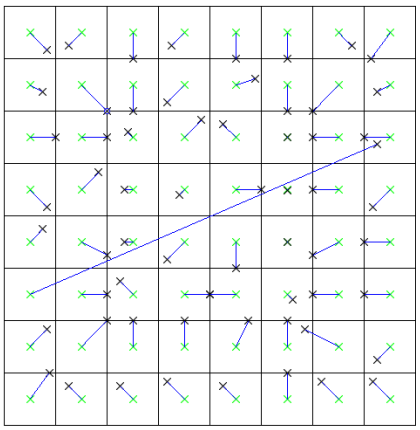

(c) $\mathcal{F}_3$

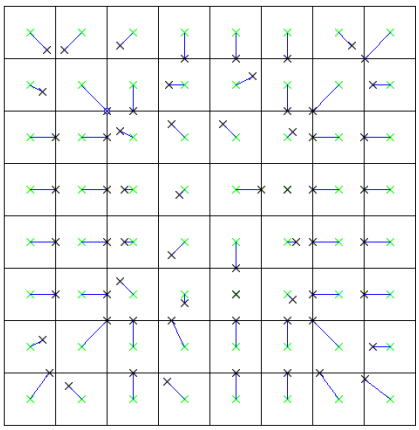

(d) $\mathcal{F}_4$

Figure 11: Localization maps with C_3 depending on modes selection (green cross: impact point, black cross: estimate).

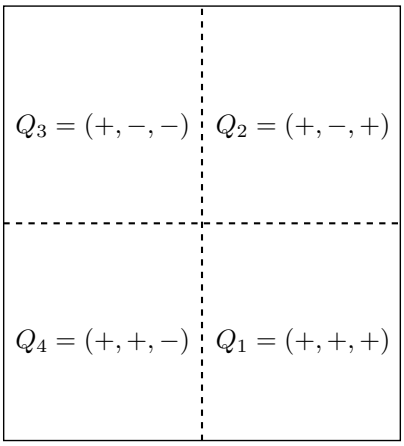

Figure 12: Division of the plate in quadrants depending on mode shapes signs.

5.3.3. Impulse intensity predictions

The impulse intensity is defined as the integral of the applied load history in absolute value (see section 2.1). Therefore, the impulse intensity estimate $\hat{f}$ (see section 3.4) must be compared to the area A of the applied load history under its curve (expressed in N.s). Figure 13 shows the correlations between estimated impulse intensity, noted f on the plot, and A. Only the impulse estimates associated to the best localization results are displayed, namely by using $\mathcal{F}_4$ (see Table 3). There is a good correlation between $\hat{f}$ and A (r=+0.8), meaning that the procedure is robust for estimating impulse intensity as well.

However, it is observed that all the estimates are below the bisector, meaning that the estimate $\hat{f}$ is always lower than A. The slopes of the linear curves are indeed closer to 0.7 than to expected 1. The most inaccurate estimates of f either correspond to impacts applied on the corners, or to applied load histories that cannot be modelled with a Dirac function. Figure 14a shows that the load histories corresponding to the red crosses displayed in Figure 13a are spiky with multi-peaks. Therefore, the impact durations may not be short enough to use the impulse response approximation (3). On the other hand, Figure 14b shows that the nearest estimates from the bisector, displayed with green crosses in Figure 13a, correspond to rather smooth load histories with a very short duration ($\approx$ 2ms). Therefore, the procedure is accurate for estimating the intensity of a Dirac-like impact.

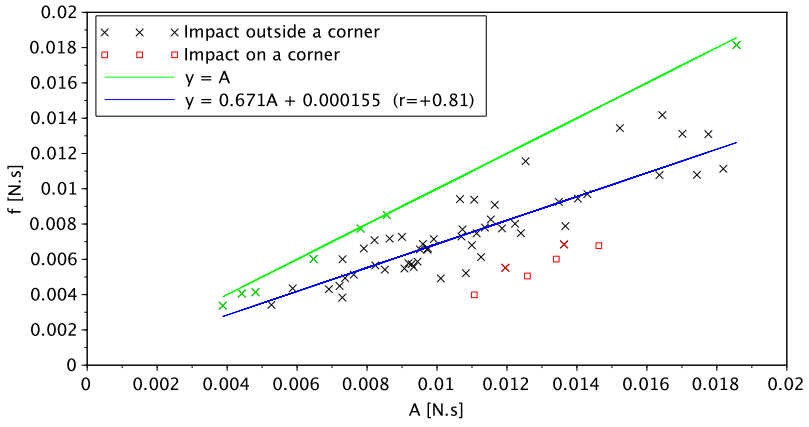

(a) C_1

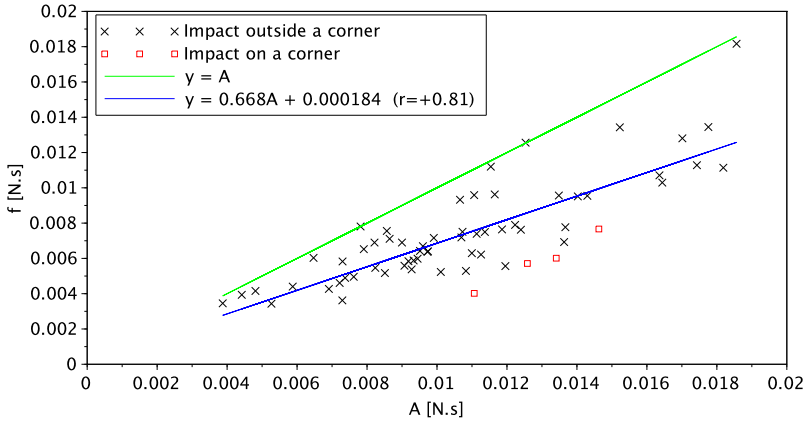

(b) C_2

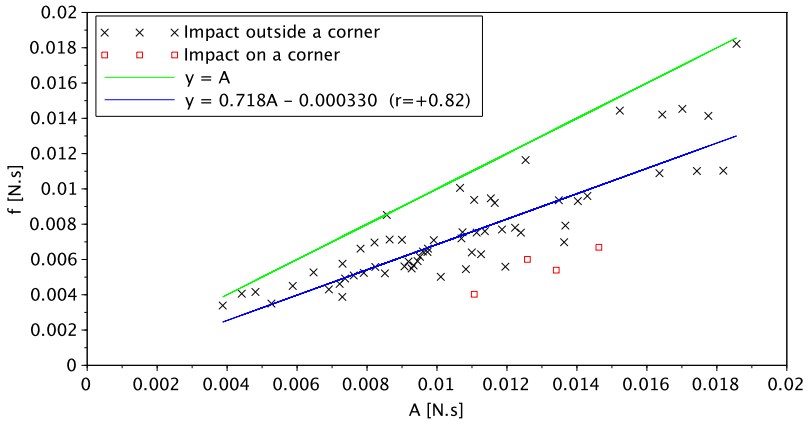

(c) C_3

Figure 13: Correlation between impulse intensities $\hat{f}$ estimated by using $\mathcal{F}_4$ and the integrals A of associated applied load histories. The green line corresponds to a perfect estimation of the force amplitude.

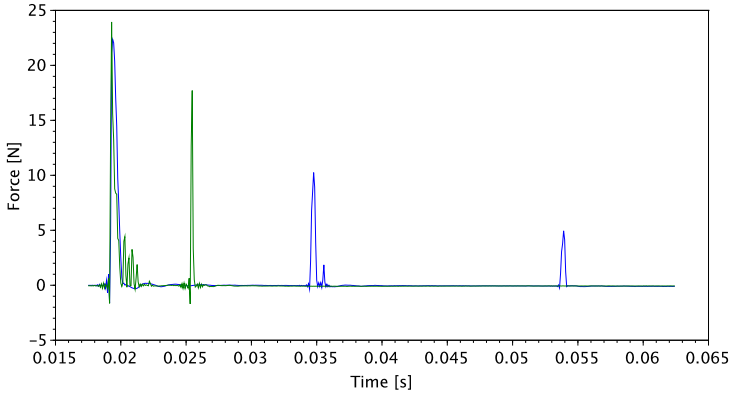

(a) Multi-peaks load histories corresponding to the two red crosses displayed on Figure 13a (estimates far from the bisector).

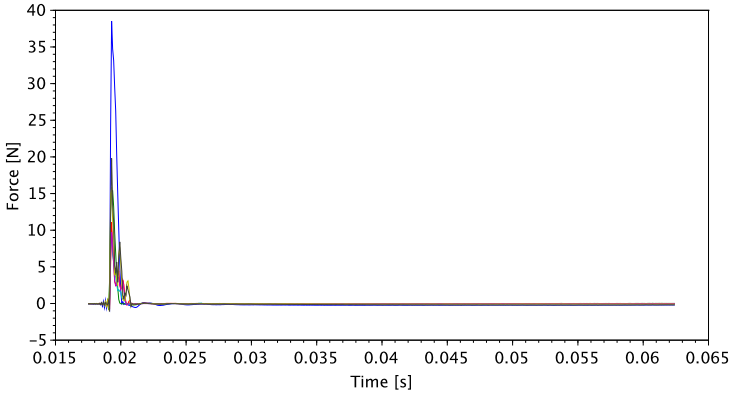

(b) Single-peak load histories corresponding to the green crosses displayed on Figure 13a (estimates near the bisector).

Figure 14: Influence of the load history shape on the estimation of the impulse intensity.

5.4. Discussion

Validity of a-o conditions. The robustness of the proposed technique depends on the a-o coefficient μ_p defined in section 4.3. The evaluation of μ_p by considering $\mathcal{F}_1$ or $\mathcal{F}_4$ respectively gives 0.012 and 0.043 (< 1). The normalized matrices $\mathbf{A_1}$ and $\mathbf{A_4}$, associated to $\mathcal{F}_1$ and $\mathcal{F}_4$, computed with the parameters in Table 2 are:

$$\mathbf{A_1} = \begin{bmatrix} 0.25 & -0.0011 & -0.00068 \\ -0.0011 & 1 & -0.0094 \\ -0.00068 & -0.0094 & 0.86 \end{bmatrix} \tag{43}$$

$$\mathbf{A_4} = \begin{bmatrix} 0.16 & 0.00069 & -0.00043 & -0.00051 & 0.00051 & 0.00025 \\ & 0.63 & -0.0059 & -0.0002 & 0.0020 & -0.000073 \\ & & 0.54 & -0.0024 & -0.0018 & 0.0021 \\ & & & 0.79 & -0.012 & 0.013 \\ & & (\text{sym.}) & & 0.77 & -0.0069 \\ & & & & & 1 \end{bmatrix} \tag{44}$$

Both $\mathbf{A_1}$ and $\mathbf{A_4}$ are strictly diagonally dominant (see section 4.3). The condition number in 2-norm of $\mathbf{A_k}$ can be computed as a function of the measurement duration D. Figure 15 shows that the prediction (36)

agrees well with the true condition number of $\mathbf{A_k}$ when D is large enough. Therefore a-o conditions are valid for this experimental use-case.

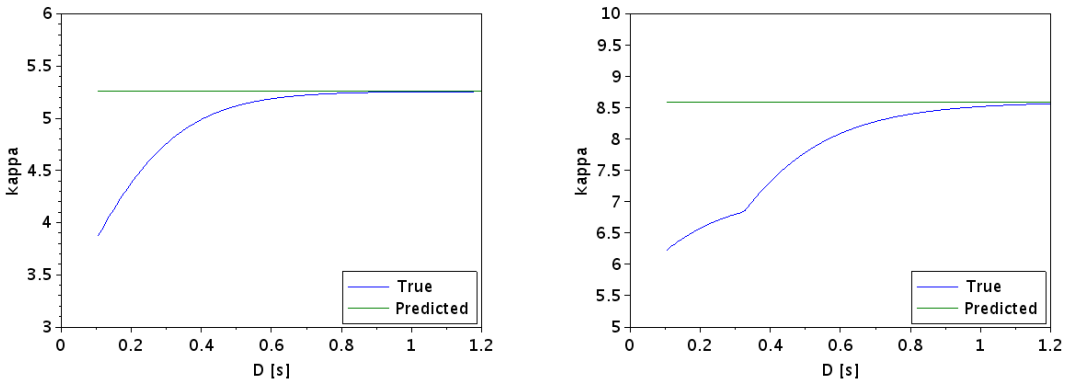

(a) $\mathcal{F}_1$ (b) $\mathcal{F}_4$

Figure 15: Evolution of the condition number $\kappa_a(\mathbf{A}_k, C_1)$ depending on measurement duration D and DMF selection.

Localization accuracy. The localization results depend on the accuracy of the modal ponderation estimations. Figure 16 shows an example of a frequency content reconstruction of acceleration measurements. It is observed that the modal ponderations of the modes in $\mathcal{F}_4$ are correctly captured, even if the truncation error seems large (modes up to 2.5kHz are excited). As suggested in section 4.2, it is important to keep a sufficient number of modes in the analysis to correctly estimate the ponderations of the discriminating vibration modes. Otherwise the truncation error may be too large.

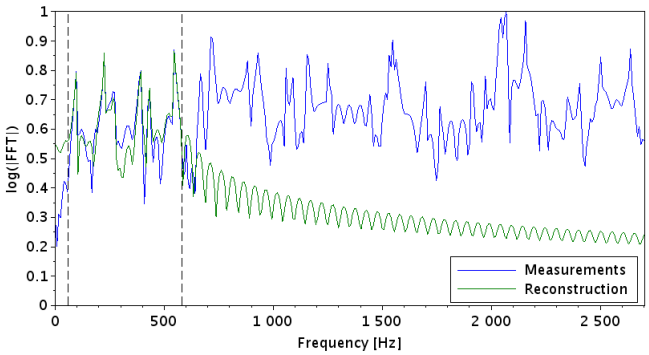

Figure 16: Reconstruction of $\mathcal{F}_4$ frequency band [60Hz,580Hz].

Implementation for a more complex structures. The general procedure is described in Figure 5. The most difficult step is to identify some mode shapes of the structure. This can be done numerically with a reliable finite element model of the structure or experimentally. Then, discriminating vibration modes can be identified and sensors can be adequatly positioned. Furthermore, it is experimentally observed that the proposed approach is more sensitive to errors on natural frequencies than to errors on damping ratios. Hence the implementation of this technique on a structure operating in a complex environment should include a calibration step to use actual natural frequencies of the selected DMF.

6. Conclusion

An inverse technique is presented in this study for quickly localizing a Dirac-like impact and for estimating its intensity from vibration measurements. The identification is performed by estimating a few modal ponderations from acceleration measurements of a single point on the structure. Compared to previous studies on modal ponderations, general rules are provided to select the appropriate vibration modes in the analysis and to position the sensor on the structure. The experimental results show the validity of the proposed technique to achieve impact localization and impulse intensity estimation on a 2D structure with help of one accelerometer only.

7. Acknowledgments

The first author thanks the french National Association of Research and Technology for his support through a PhD grant (n°2016/0887). The authors are also thankful to the mathematician Prof. Saab Abou-Jaoude for all his valuable ideas.

Appendix: Proofs of section 4 properties

Let E be the vector space of continuous square integrable functions on the interval $[0, +\infty[$. Let $(.|.)_E$ be the usual scalar product on E defined by $(u|v)_E = \int_0^{+\infty} u(t)v(t)dt$. Let $\mathcal{G}^* = (g_j^*)_{1\leq j\leq p}$ be a family of p normalized modal impulse responses $g_j/\|g_j\|_E$.

Property 1. *The elements of $\mathcal{G}^*$ satisfy:*

$$\|g_j^*\|_E = 1 \qquad \textit{and for } i \neq j \qquad |(g_i^*|g_j^*)_E| \leq \mu = \frac{\eta_{Max}^2}{(1-(\eta_{Max}^2-\eta_{min}^2))(\eta_{min}^2+s^2)}$$

Proof. It is straightforward to get:

$$(g_i|g_i)_E = \frac{1}{4\eta_i\omega_{0i}^3}$$

For $i \neq j$, more developements lead to:

$$|(g_i|g_j)_E| \leq \frac{1}{4(\omega_{0i}\omega_{0j})^{3/2}} \frac{\eta_{Max}}{(1-(\eta_{Max}^2-\eta_{min}^2))(\eta_{min}^2+s^2)}$$

The property on $\mathcal{G}^*$ follows by using:

$$\frac{1}{\|g_i\|_E\|g_j\|_E} \leq 4\eta_{Max}(\omega_{0i}\omega_{0j})^{3/2}$$

□

Let's note $F = \mathbb{R}^n$ and let $\mathbf{G_j} = (g_j(t_1)\ ...\ g_j(t_n))^T$ be the j-th modal impulse response discretized in time. Let $(.|.)_F$ be the usual euclidian scalar product on F defined by $(\mathbf{U}|\mathbf{V})_F = \mathbf{U}^T.\mathbf{V}$. Let Δt be the sensor sampling period and $D = n\Delta t$ be the acquisition duration. Let's note $\mathbf{G_j^*} = \mathbf{G}_j/\|\mathbf{G}_j\|_F$ the normalized modal impulse reponses discretized in time.

Property 2. *If the measurement duration D is large enough and if the sampling period Δt is small enough then the elements $\mathbf{G_j^*}$ satisfy:*

$$\|\mathbf{G}_j^*\|_F = 1 \qquad \textit{and for } i \neq j \qquad |(\mathbf{G_i^*}|\mathbf{G_j^*})_F| \leq \mu_p = \frac{\mu+\eta_{Max}^2}{1-\eta_{Max}^2}$$

Proof. Recall that $D = n\Delta t$. The first step is to prove that $(u|v)_E$ can be approximated by $\Delta t(\mathbf{U}|\mathbf{V})_F$ at a given tolerance if the measurement duration D and the sampling frequency $1/\Delta t$ are large enough:

$$\begin{gathered}\forall\epsilon > 0, \exists D^* > 0, \exists n^*(D) > 0,\\ (D \geq D^*, n \geq n^*(D) \Rightarrow |\Delta t(\mathbf{U}|\mathbf{V})_F - (u|v)_E| \leq \epsilon)\end{gathered}$$

This property is then applied to the family $(g_i)_{1\leq i\leq p}$ of modal impulse responses:

$$\begin{gathered}\forall\epsilon > 0, \exists D^* > 0, \exists n^*(D) > 0,\\ (D \geq D^*, n \geq n^*(D) \Rightarrow \forall i,j \in [\![1,p]\!], |\Delta t(\mathbf{G_i}|\mathbf{G_j})_F - (g_i|g_j)_E| \leq \epsilon)\end{gathered}$$

By noting $\mathbf{G_i'} = \frac{\sqrt{\Delta t}}{\|g_i\|_E}\mathbf{G_i}$ it is straightforward to show:

$$|\Delta t(\mathbf{G_i}|\mathbf{G_j})_F - (g_i|g_j)_E| \leq \epsilon \Leftrightarrow \begin{cases} 1-\epsilon/\|g_i\|_E^2 \leq \|\mathbf{G_i'}\|_F^2 \leq 1+\epsilon/\|g_i\|_E^2 \\ |(\mathbf{G_i'}|\mathbf{G_j'})_F| \leq \mu + \epsilon/(\|g_i\|_E\|g_j\|_E) \qquad \text{for } i \neq j \end{cases}$$

The property follows by noting $\mathbf{G_j^*} = \mathbf{G_j'}/\|\mathbf{G_j'}\|_F = \mathbf{G}_j/\|\mathbf{G}_j\|_F$ and by chosing $\epsilon = \eta_{Max}^2 \min_i \|g_i\|_E^2$. □

Let $\mathbf{Q}$ be the discretized measured response and assume that $\mathbf{Q}$ has a decomposition in a family of $m > p$ discretized modal impulse responses $(\mathbf{G_i})_{1\leq i\leq m}$. Let $\tilde{\mathbf{Q}}$ be the discretized model response defined with (3). Let's note $\mathbf{Q_e} = \mathbf{Q} - \tilde{\mathbf{Q}}$ the modelization error and let $\hat{\mathbf{Q}}$ be the orthogonal projection of $\mathbf{Q}$ on $\text{span}((\mathbf{G_i})_{1\leq i\leq p})$. Recall that $\hat{\mathbf{Q}}$ is obtained with the least-squares procedure (see section 2.3). Let $\mathbf{X}, \tilde{\mathbf{X}}, \mathbf{X_e}$ and $\hat{\mathbf{X}}$ be the vectors of the components of $\mathbf{Q}, \tilde{\mathbf{Q}}, \mathbf{Q_e}$ and $\hat{\mathbf{Q}}$ in $(\mathbf{G_i})_{1\leq i\leq m}$.

Property 3. *Let μ_m be the a-o coefficient associated to $(\mathbf{G_i^*})_{1\leq i\leq m}$. Then:*

$$\|\hat{\mathbf{X}} - \tilde{\mathbf{X}}\|_\infty \leq \mu_m(m-p)\|\mathbf{X_e}\|_\infty$$

Proof. Let's note $\mathbf{N_i} = \mathbf{G_i^*}$. Then $\mathbf{Q} = \sum_{i=1}^m x_i\mathbf{N_i}$, $\tilde{\mathbf{Q}} = \sum_{i=1}^p x_i\mathbf{N_i}$ and $\hat{\mathbf{Q}} = \sum_{i=1}^p \hat{x}_i\mathbf{N_i}$. Recall that $\hat{\mathbf{Q}}$ is the orthogonal projection of $\mathbf{Q}$ on $\text{span}(\mathbf{N_1}, ..., \mathbf{N_p})$. Hence:

$$\begin{aligned}\forall j = 1, ..., p \qquad &\left(\mathbf{Q} - \hat{\mathbf{Q}} \mid \mathbf{N_j}\right) = 0 \\ &\left(\sum_{i=1}^m x_i\mathbf{N_i} - \sum_{i=1}^p \hat{x}_i\mathbf{N_i} \mid \mathbf{N_j}\right) = 0\end{aligned}$$

Therefore:

$$\begin{aligned}\forall j = 1, ..., p \qquad \sum_{i=1}^p \hat{x}_i \left(\mathbf{N_i} \mid \mathbf{N_j}\right) &= \sum_{i=1}^m x_i \left(\mathbf{N_i} \mid \mathbf{N_j}\right) \\ &= \sum_{i=1}^p x_i \left(\mathbf{N_i} \mid \mathbf{N_j}\right) + \sum_{i=p+1}^m x_i \left(\mathbf{N_i} \mid \mathbf{N_j}\right)\end{aligned}$$

Let $\mathbf{N_{p,p}}$ be the matrix of general term $(\mathbf{N_i} \mid \mathbf{N_j})$ with $i, j \in [\![1, p]\!]$. Let's note $q = m - p$ and let $\mathbf{N_{p,q}}$ be the matrix of general term $(\mathbf{N_i} \mid \mathbf{N_j})$ with $i \in [\![1, p]\!]$ and $j \in [\![p+1, m]\!]$. Let's note $\hat{\mathbf{X}} = (\hat{x}_1 \ ... \ \hat{x}_p)^T$ and $\mathbf{X} = (\tilde{\mathbf{X}} \ \mathbf{X_e})^T$ with $\tilde{\mathbf{X}} = (x_1 \ ... \ x_p)^T$ and $\mathbf{X_e} = (x_{p+1} \ ... \ x_m)^T$. Then:

$$\mathbf{N_{p,p}}\hat{\mathbf{X}} = \mathbf{N_{p,p}}\tilde{\mathbf{X}} + \mathbf{N_{p,q}}\mathbf{X_e}$$

By definition $(\mathbf{N_i} \mid \mathbf{N_i}) = 1$ and $|\left(\mathbf{N_i} \mid \mathbf{N_j}\right)| \leq \mu_m$. For any vector $\mathbf{Y} = (y_1 \ ... \ y_l)^T$ let's note $\|\mathbf{Y}\|_\infty = \sup_i |y_i|$, and for any $k \times l$ matrix $\mathbf{M}$ let $\|\mathbf{M}\|_\infty = \sup_{\|\mathbf{Y}\|_\infty \leq 1} \|\mathbf{MY}\|_\infty$ be the induced matrix norm. The property follows by using the separation property of the induced norm in the previous relation. □

An appropriate scaling c independent of m then leads to the relation (32).

Property 4. *Let μ_p be the a-o coefficient associated to $(\mathbf{G_i^*})_{1\leq i\leq p}$. Then:*

$$\frac{1-\eta_{Max}^2}{4\Delta t}\frac{\phi_i^2(C)}{\eta_i\omega_{0i}^3} \leq A_{ii} \leq \frac{1+\eta_{Max}^2}{4\Delta t}\frac{\phi_i^2(C)}{\eta_i\omega_{0i}^3}$$

And for $i \neq j$

$$|A_{ij}| \leq \mu_p \frac{1-\eta_{Max}^2}{4\Delta t}\frac{|\phi_i(C)\phi_j(C)|}{(\eta_i\eta_j)^{1/2}(\omega_{0i}\omega_{0j})^{3/2}}$$

Proof. By noticing that the general coefficient of matrix $\mathbf{A}$ expresses as:

$$A_{ij} = \phi_i(C)\phi_j(C)(\mathbf{G_i}|\mathbf{G_j})_F = \frac{\phi_i(C)\phi_j(C)}{\Delta t}\|\mathbf{G}_i'\|_F\|\mathbf{G}_j'\|_F\|g_i\|_E\|g_j\|_E(\mathbf{G_i^*}|\mathbf{G_j^*})_F$$

□

It follows from the previous property that $\mathbf{A}$ takes a strictly diagonally dominant form if μ_p is small enough and if $C \notin \cup_{i=1}^p L_i(0)$.

References

[1] H. Inoue, J. Harrigan, S. Reid, Review of inverse analysis for indirect measurement of impact force, Applied Mechanics Reviews, American Society of Mechanical Engineers 54 (2001) 503–524.

[2] S. Ahmari, M. Yang, Impact location and load identification through inverse analysis with bounded uncertain measurements, Smart Materials and Structures 22 (2013) 085024.

[3] G. Zhao, H. Hu, S. Li, L. Liu, K. Li, Localization of impact on composite plates based on integrated wavelet transform and hybrid minimization algorithm, Composite Structures 176 (2017) 234–243.

[4] J. Frieden, J. Cugnoni, J. Botsis, T. Gmür, Low energy impact damage monitoring of composites using dynamic strain signals from fbg sensors – part i: Impact detection and localization, Composite Structures 94 (2012) 438–445.

[5] C. Chang, C.-T. Sun, Determining transverse impact force on a composite laminate by signal deconvolution, Experimental Mechanics 29 (1989) 414–419.

[6] P. Hansen, Deconvolution and regularization with Toeplitz matrices, Numerical Algorithms 29 (2002) 323–378.

[7] Z. Chen, T. Chan, A truncated generalized singular value decomposition algorithm for moving force identification with ill-posed problems, Journal of Sound and Vibration 401 (2017) 297–310.

[8] A. Tikhonov, V. Arsenin, Solutions of ill-posed problems, Winston-Wiley, 1977.

[9] K. Khalori, L. Ye, S. Mustapha, J. Li, B. Li, Reconstruction and analysis of impact forces on a steel-beam-reinforced concrete deck, Experimental Mechanics 56 (2016) 1547–1558.

[10] P. Hansen, Analysis of discrete ill-posed problems by means of the L-curve, Journal of the Society for Industrial and Applied Mathematics 34 (1992) 561–580.

[11] E. Jacquelin, A. Bennani, P. Hamelin, Force reconstruction: analysis and regularization of a deconvolution problem, Journal of Sound and Vibration 265 (2003) 81–107.

[12] G. Golub, M. Heath, G. Wahba, Generalized cross-validation as a method for choosing a good ridge parameter, Technometrics 21 (1979) 215–223.

[13] H. Choi, A. Thite, D. Thompson, Comparison of methods for parameter selection in tikhonov regularization with application to inverse force determination, Journal of Sound and Vibration 304 (2007) 894–917.

[14] D. Donoho, For most large underdetermine systems of linear equations the minimal l1-norm solution is also the sparsest solution, Communications on pure and applied mathematics 59 (2006) 797–829.

[15] B. Qiao, X. Zhang, J. Gao, R. Liu, X. Chen, Sparse deconvolution for the large-scale ill-posed inverse problem of impact force reconstruction, Mechanical Systems and Signal Processing 83 (2017) 93–115.

[16] Q. Li, Q. Lu, Impact localization and identification under a constrained optimization scheme, Journal of Sound and Vibration 366 (2016) 133–148.

[17] L. Vladislav, R. Zemcik, T. Kroupa, J. Bartosek, Reconstruction of impact force on curved panel using piezoelectric sensors, Procedia Engineering 48 (2012) 367–374.

[18] J. Briggs, M.-K. Tse, Impact force identification using extracted modal parameters and pattern matching, International Journal of Impact Engineering 12 (1991) 361–372.

[19] B.-T. Wang, C.-H. Chiu, Determination of unknown impact force acting on a simply supported beam, Mechanical Systems and Signal Processing 17 (2003) 683–704.

[20] Y. Zhong, J. Xiang, H. Gao, Y. Zhou, Impact energy level assessment of composite structures using music-ann approach, Structural Control and Health Monitoring 23 (2016) 825–837.

[21] M. Géradin, D. J. Rixen, Mechanical Vibrations - Theory and Application to Structural Dynamics, Third Edition, Wiley, 2015.

[22] G. Strang, Introduction to Linear Algebra, Fifth Edition, Wellesley-Cambridge Press, 2016.

[23] D. Goutaudier, Impact identification technique for a structure with weakly damped and well-separated low frequency vibration modes, PhD thesis, Conservatoire National des Arts et Métiers de Paris, 2019.

[24] P. Spiteri, Algorithmes numériques pour la résolution de grands systèmes, Techniques de l'ingénieur, 2002.

[25] O. Robin, J.-D. Chazot, R. Boulandet, M. Michau, A. Berry, N. Atalla, A plane and thin panel for representative simply supported boundary conditions for laboratory vibroacoustic tests, Acta Acustica United with Acustica 102 (2016) 170–182.

[26] A. Leissa, Vibration of plates, NASA SP-160, 1969.